THE JOURNAL OF PHYSICAL CHEMISTRY B

ARTICLE

pubs.acs.org/JPCB

Structural and Electronic Models of the Water Oxidizing Complex in the S_0 State of Photosystem II: A Density Functional Study.

Adrian R. Jaszewski, Rob Stranger, and Ronald J. Pace*

Research School of Chemistry, College of Science, Australian National University, Canberra ACT 0200, Australia

Supporting Information

ABSTRACT: Large size (228 atom, 229 atom for protonated form) molecular models of the oxygen evolving complex of photosystem II (OEC), with a complete set of ligating amino-acids, the redox-active tyrosine Y_Z, and proton/water transfer channels terminating at the water oxidizing Mn/Ca cluster, are constructed based on the highest available resolution X-ray diffraction structures of the protein and our previous density functional theory (DFT) studies of isolated metal cluster model structures. Geometries optimized using the general gradient approximation (GGA) or hybrid density functionals are compared with high-resolution extended X-ray absorption fine structure (EXAFS) spectroscopic data and show that an antiferromagnetic configuration of the Mn centers in the cluster gives computed metal−metal distances in excellent agreement with experiment. The excitation energies predicted by time-dependent density functional theory (TDDFT) calculations for truncated 106 atom and 78 atom structures derived from the large models show that a previously proposed III−III−III−II oxidation pattern of the Mn atoms agrees very well with the X-ray absorption near-edge structure (XANES) observed for the S_0 state of the OEC. This supports a "low" Mn oxidation state paradigm for the OEC, when a realistic protein imposed environment for the catalytic metal cluster is used in calculations. The probable protonation sites in the cluster and roles of the proton/water transfer channels are discussed in light of the computational results.

1. INTRODUCTION

The reaction center of PSII, a multisubunit complex present in the thylakoid membrane of cyanobacteria, algae, and higher plants, catalyzes the oxidation of water to oxygen.[1−3] Light absorption initiates electron transfer from a specialized chlorophyll complex, P680, to the neighboring pheophytin (Pheo) and then to the primary quinone, Q_A, forming a semiquinone radical $Q_A^{\bullet-}$. Through a series of further steps, electrons are conveyed to Photosystem I and subsequently to the CO_2-fixing reactions of the Calvin cycle. The oxidized primary donor, $P680^+$, is reduced by the redox active tyrosine, Y_Z, and the resulting $Y_Z^{\bullet}$ radical is in turn reduced by electrons withdrawn from the $Ca(Mn)_4$-containing oxygen-evolving complex that provides the substrate-binding sites in the water-splitting process. The water oxidizing complex (WOC), consisting of this Mn cluster ligated to the surrounding amino acids and redox-active tyrosine, produces molecular oxygen with a periodicity of four single photon turnovers of P680, permitting a description of the whole cycle in terms of five intermediate states, S_i, (i = 0−4) called S states. Formally, the cycle begins with S_0, however S_1 is known to be to be dark-stable[4] while S_4 is transient.

The mechanism by which water is oxidized and the detailed structural arrangement of the WOC remain unclear, despite intense multidisciplinary studies[5−8] and recent X-ray structural determinations.[9−11] Although it is established that the WOC contains four Mn and one Ca atom, the overall shape of the cluster, the nature of the metal bridging ligands, the exact number of ligating amino acid residues, the sites binding substrate water molecules, and the manganese oxidation pattern for any given S state are still areas of contention.[5−12] Moreover, different X-ray crystallographic studies[9−11] lead not only to somewhat inconsistent geometries of the Mn/Ca cluster, but they do not unequivocally identify proton and water transfer channels,[13−17] nor the precise position of the Cl^- ion,[18,19] which is a known cofactor required for water oxidation in the WOC.[20] This paper is a continuation of our previous density functional theory (DFT) computational studies on the structure of the WOC[21−24] which have addressed the observed variation in manganese positions in the XRD experiments, as well as our recent studies on the utility of time-dependent DFT in rationalizing the dependence of X-ray absorption near-edge spectroscopy (XANES) edge energies on the oxidation state and ligand environment in Mn compounds.[25,26]

The metal X-ray absorption spectroscopy (XAS) energy (usually the K edge) is commonly used to determine the oxidation state of Mn atoms in a wide range of biological systems of different origin.[27−29] The observed value of the edge energy is dependent not only on the metal oxidation state itself but also on the nature of the ligands and their organization. Therefore, agreement between the XANES characteristics observed experimentally and predicted theoretically can be used as an important

Received: January 3, 2011
Revised: February 28, 2011
Published: March 24, 2011

Scheme 1. Schematic Diagram of the Amino-Acid Ligation Pattern for the B3LYP Optimized Model of the WOC

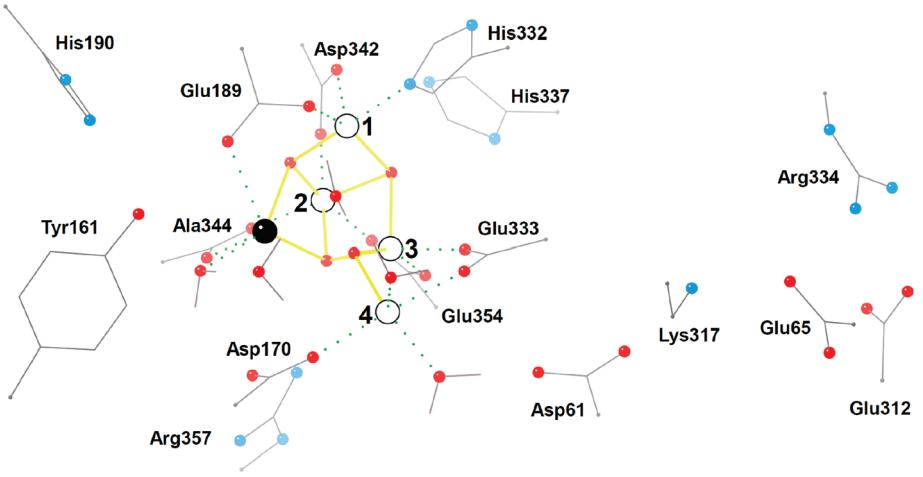

factor to validate the structural and electronic correctness of WOC models, if all relevant factors influencing the edge properties are duly accounted for. Recently we have compared TDDFT results on a class of model Mn_4/Ca clusters, which reproduce many aspects of the functional WOC site, with the full range of Mn K-edge energy data available for PSII in its intermediate, isolatable S states.[30] This has allowed us to identify model structures corresponding to particular S states and to propose the mean overall oxidation state of the Mn atoms in the tetramanganese cluster during functional turnover. This ranges from 2.75 for S_0, 3.00 for S_1, 3.25 for S_2, up to 3.50 for the S_3 state.[30] This range is consistently below other estimates proposed from purely empirical comparisons.[31] Interestingly, the TDDFT calculations showed that somewhat different edge energies could be expected for the same Mn oxidation pattern in broadly similar cluster geometries, each individually consistent in its metal locations with a particular XRD structure of PS II. Moreover this variation could be correlated with the observed range in published Mn K edge data for the PS II.[30] The range was greatest for S_1, but the results clearly indicated that the S_0 state was most prescriptive in distinguishing between different paradigms for the mean Mn oxidation levels in functional PS II.

Our computational studies to date, although consistent with a wide range of experimental data on the enzyme WOC site, have involved isolated model Mn_4/Ca clusters with water molecules, oxo bridges, and ligand species mimicking the metal bonding environment in the protein, as currently understood. They are, however, otherwise unconstrained. Given the demonstrated sensitivity of Mn K edge energies to details of metal site geometry, which our calculations reveal, it is vital that our conclusions be tested in a structural environment as far as possible replicating the protein embedded active WOC site, notably in the S_0 state. That is the purpose of this paper. Further we make a preliminary computational examination of putative proton/water channels to the cluster, which have been proposed from structural analysis[13−17] and suggested as mechanistically important by our earlier modeling studies.[23,24] We examine S_0 state geometries derived from both generalized gradient approximation (GGA) and hybrid density functionals, modeling the constraints imposed by the surrounding protein framework, as derived from the highest resolution published XRD structures. The systems studied contain up to 229 atoms and are the largest and most extensive WOC models calculated so far by pure DFT methods.

2. METHODOLOGY

An initial geometry for DFT optimization was derived from the protein framework revealed by the recent Berlin XRD structures.[11,14] The 2.9−3.0 Å resolution of these studies is sufficient to indicate a possible topology of the Mn_4Ca cluster, as well as the number and type of ligating amino-acids, but still cannot define the detailed geometry of the WOC, notably the number and location of presumed oxo bridges between metal atoms. Therefore, the positions of the bridging ligands as well as five binding water molecules in the initial structure were chosen according to the findings of our recent DFT studies,[21−24,30] specifically resembling the type **II** (Hyogo-like) rather than type **I** (Berlin-like) metal arrangement, which favorably reproduces extended X-ray absorption fine structure (EXAFS) derived experimental metal−metal distances. This model differs from those suggested by other groups,[32−36] as it possess fewer (four) oxo bridges between manganese atoms, which in turn stabilizes lower Mn oxidation states. On the basis of the conclusions from our recent TDDFT studies,[30] a mean oxidation level of 2.75 for the cluster Mn atoms is initially assumed for the WOC in the S_0 state.

The initial structure (see Scheme 1) contains His332, Asp342, and Glu189 to reproduce the ligand environment of Mn1, as well as neighboring His337 which could potentially interact with the oxo bridge between Mn1, Mn2, and Mn3. The ligation sphere of Mn2 is saturated by addition of Glu354 and Ala344. Further inclusion of Glu333 and Asp170 is necessary for a correct description of the ligand environment of Mn3 and Mn4. To complete the ligation sphere of the Mn_4Ca cluster, Ala344 at the C-terminus of the D1 polypeptide is also included in the calculations, together with Arg357. To account for interactions with Y_Z, which may be especially significant in future studies of higher oxidized states of the WOC, Tyr161 and His190 have been also incorporated. On the other side of the Mn_4Ca cluster, several amino-acids forming a potentially important channel for proton transfer have been also included, namely Asp61, Lys317, Glu65, Arg334, and Glu312. The likely significance of this channel has been highlighted by our recent calculations on

dx.doi.org/10.1021/jp200053n |J. Phys. Chem. B 2011, 115, 4484–4499

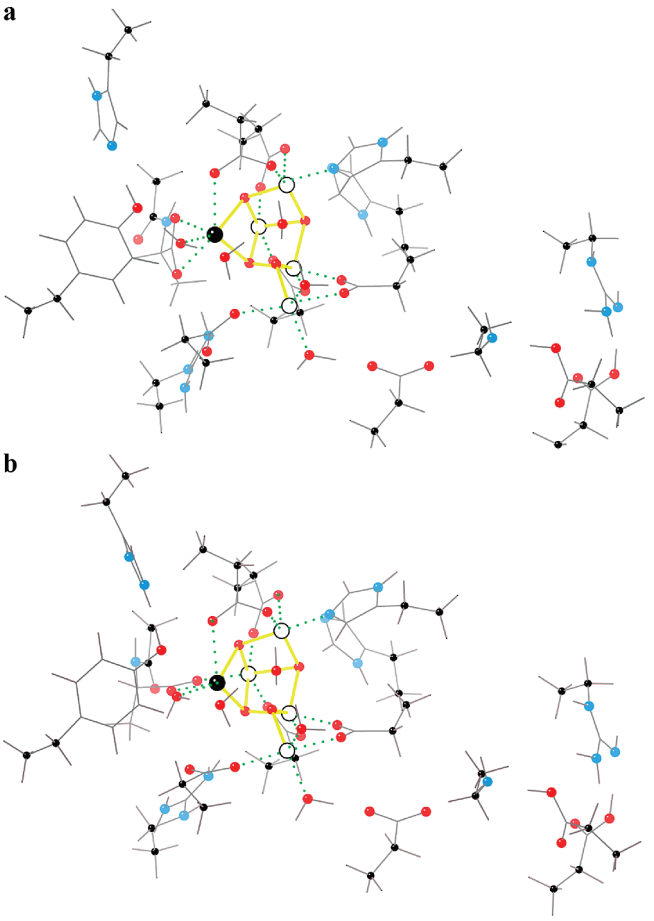

Figure 1. Computational models of the WOC optimized using the BP86 (a) and B3LYP (b) functionals. Large white spheres Mn; large black sphere Ca; medium red spheres O; medium blue spheres N; black spheres C atoms of terminal amino-acid groups frozen during optimization.

isolated cluster models of the WOC.[23,24,30] Except for the terminal and therefore flexible Ala344, which was included together with the peptide bond to the previous amino-acid and terminated with a methyl group, all other amino-acids were considered up to the second carbon from the functional/ligating group only, which was saturated with three methyl hydrogens added automatically at a distance of 1.1 Å by ArgusLab software.[37]

This system containing 228 atoms (Figure 1) was partially optimized, keeping the first carbon from the functional/ligating group and terminal methyl group of each amino-acid frozen—to mimic constraints imposed by the protein framework—and allowing the Mn_4Ca cluster together with all water molecules and all functional/ligating groups of all amino-acids to be freely optimized—to account for an assumed flexibility of the system and uncertainty of the XRD structural determination.[38] The reported XRD structures are for PSII in a nominal S_1 configuration, but rapid reduction of higher metal oxidation states by photoelectrons during the data collection means that the actual reported metal configurations correspond to Mn in indeterminate, but probably reduced, oxidation states.

The geometry optimizations at a GGA level were performed with the ADF package[39] using the local density approximation by Vosko, Wilk, and Nusair[40] (VWN) and gradient corrections proposed by Becke[41] (B) and Perdew[42] (P86) combined with the

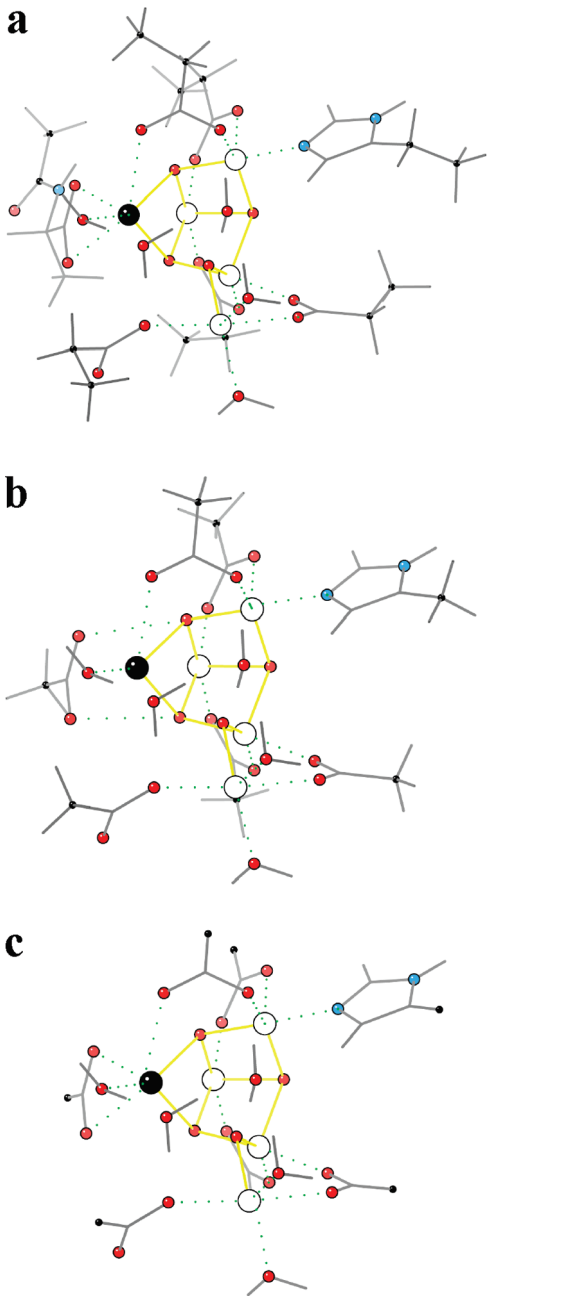

Figure 2. Large size 106 atom (a), medium size 78 atom (b), and small size 57 atom (c) structures of the WOC. Large white spheres Mn; large black sphere Ca; red spheres O; blue spheres N; small black spheres C and/or H atoms of amino-acid residues reoptimized prior to the TDDFT calculations.

all-electron Slater-type basis set of triple-ζ plus polarization (TZP) quality.[43] No symmetry constrains were set during geometry optimizations. Calculations were performed within the unrestricted scalar ZORA relativistic formalism.[44]

Hybrid density functional (HDF) optimizations were performed without any symmetry constrains with the Gaussian03 package,[45] using the unrestricted formalism and B3LYP hybrid density functional,[46] combined with the basis set of Wachters[47] augmented with additional f exponents[48] for Mn ([62111111/331211/3111/1]), the [63111111/321111/2111] contracted DZVP basis set of Godbout[49] for Ca, and the D95(d,p) basis

dx.doi.org/10.1021/jp200053n |J. Phys. Chem. B 2011, 115, 4484–4499

Table 1. Metal−Ligand Structural Properties (Bond Lengths in Angstroms) Derived from the DFT Calculations on the WOC of PSII at the S_0 State

properties	BP86 frozen AAAA	BP86 frozen ABBA	B3LYP frozen AAAA	BP86 free medium AAAA	B3LYP free medium AAAA
r(Mn1−N(HIS332))	2.08	2.08	2.13	2.09	2.12
r(Mn1−O(ASP342))	2.24	2.25	2.18	2.19	2.18
r(Mn1−O(GLU189))	2.00	2.00	2.03	2.03	2.05
r(Ca−O(GLU189))	2.73	2.71	2.78	3.90[a]	2.44
r(Mn2−O(ASP342))	1.97	1.98	1.98	1.99	2.02
r(Mn2−O(GLU354))	2.05	2.04	2.08	2.02	2.01
r(Mn2−O(ALA344))	2.48[b]	2.48[b]	2.16	2.43[b]	2.17
r(Ca−O(ALA344))	2.66	2.67	2.40	2.43	2.32
r(Mn3−O(GLU354))	2.00	2.02	2.00	2.03	2.04
r(Mn3−O(GLU333))	2.02	2.01	2.02	2.02	2.05
r(Mn4−O(GLU333))	2.24	2.27	2.21	2.07	2.13
r(Mn4−O(ASP170))	2.26	2.30	2.23	2.07	2.07
r(Mn4−O(H2O))	2.30	2.33	2.28	5.20[c]	2.55
r(Mn4−O(H2O′))	2.14	2.11	2.14	2.12	2.25
r(Ca−O(H2O″))	2.40	2.40	2.41	2.42	2.41

[a] Oxygen of GLU189 interacts with water molecules instead of Ca atom. [b] Bond distance between oxygen of ALA344 and Ca instead of Mn2 atom. [c] Oxygen of water interacts with hydrogen of other water molecule instead of Mn4 atom.

set of Dunning[50] for all other atoms. All electrons were included in the calculations.

To test the effect of the protein network on the Mn_4Ca cluster, full geometry optimizations have been performed both at the GGA and HDF level, starting from the relevant partially optimized structures, modified by a reduction of the number of amino-acids included. Only those groups directly ligated to the Mn_4Ca cluster were retained—with replacement of all terminal ethyl groups by methyl groups (including Ala344). This defined a set of "medium size" 78 atom structures, analogous to those we have previously considered.[30]

TDDFT calculations were performed at the BP86/TZP level using ADF, as described previously.[25,26,30] In all TDDFT calculations, the adiabatic local density approximation was employed for the XC kernel,[51] and only spin-allowed excitations were considered. The energies of the Mn 1s core electron excitations to orbitals lying from ca. 20 eV up to ca. 120 eV above the highest occupied molecular orbital (HOMO)/singly occupied molecular orbital (SOMO) levels were calculated. This one-electron excited configuration space was divided into subspaces, allowing computations on 70−140 core excitations to be performed in one computational job. Excitations from each individual 1s Mn orbital were calculated separately. All excitation energies were first sorted by their oscillator strengths, *f*, and only data with *f* higher than 10^{-4} au were included in the subsequent analysis. The calculated spectra were convoluted with Gaussian functions in order to determine a mean edge energy corresponding to the position of the envelope maximum. The appropriate full width at half-maximum (fwhm) values employed for the Gaussian functions were between 10 and 25 eV and do not represent actual effective line-widths, as discussed previously.[26]

Since TDDFT calculations could not be performed directly on the largest (228 atom) optimized models of the WOC due to their extended size, geometries were further modified by limiting the amino-acids solely to those directly ligated to the Mn_4Ca cluster and by keeping the optimized positions of the cluster, ligating water molecules, and functional/ligating groups frozen while reoptimizing the remaining ethyl/methyl groups with ADF ("large size" 106 atom structure). To test further the effect of the ligand size approximation on the TDDFT energies, structures were further reduced by replacing terminal ethyl groups by methyl groups (including Ala344, medium size 78 atom structures) or hydrogens (small size 57 atom structures) and allowing for the reoptimization of the terminal atoms with ADF (Figure 2).

The structural effect of a single protonation of the Mn_4Ca cluster was tested at the HDF level, by performing partial reoptimizations of the relevant 229 atoms models containing an additional proton attached to any binding water molecule, any of the oxo bridges, or to any carboxylic group of an amino-acid singly coordinated to the Mn atoms of the cluster (Asp170, Glu189, Ala344).

3. RESULTS AND DISCUSSION

3.1. Structural Considerations. The WOC model geometries optimized at the BP86/TZP and BP3LYP/Wachters+DZVP+D95(d,p) levels are shown in Figure 1. The main difference between GGA and HDF results is that the latter predicts the terminal carboxylic group of Ala344 to ligate both Mn2 and Ca, while BP86 favors bidentate ligation to Ca (Table 1). Analogous differences exist within the experimental data, where the London XRD structure shows possible ligation by Ala344 to Ca only,[10] whereas the Berlin XRD structure indicates Ala344 binding to both Mn2 and Ca atoms.[11] Fourier transform infrared (FTIR) difference studies[52] indicate a lack of ligation to Ca, and recent ^{13}C ENDOR studies[53] suggest ligation by Ala 344 to at least one Mn atom. We have previously suggested,[21−24,30] based on a number of criteria, that the WOC region of PSII is somewhat variable in its detailed structure, even in "functional" samples and that this variability may also be present in the protein as crystallized under different conditions. The computational results suggest that a preference for "Berlin" over "London" structural organization of the flexible C terminal region of the D1 peptide is probably marginal, driven by the preferred ligation mode of the C terminal carboxylate under particular conditions. In our modeling to date, the C terminus is flexible only back to the penultimate

Table 2. Structural Properties (Bond Lengths in Angstroms, Angles in Degrees) of the Manganese Cluster Derived from the DFT Calculations

properties	BP86 frozen AAAA	BP86 frozen ABBA	B3LYP frozen AAAA	BP86 free medium AAAA	B3LYP free medium AAAA
r(Mn1−Mn2)	2.77	2.72	2.87	2.74	2.89
r(Mn2−Mn3)	2.78	2.78	2.87	2.80	2.91
r(Mn1−Mn3)	3.33	3.26	3.30	3.54	3.39
r(Mn3−Mn4)	3.05	2.85	3.12	3.15	3.13
r(Mn1−Mn4)	5.42	5.29	5.46	5.73	5.66
α(Mn[123])	73.7	72.8	70.3	79.2	71.5
α(Mn[234])	144.6	145.1	142.0	135.2	129.2
α(Mn[134])	116.1	119.5	116.1	117.8	120.2
α(Mn[1234])	83.7	89.5	88.5	90.7	102.2
r(Ca−Mn1)	3.54	3.53	3.44	3.65	3.43
r(Ca−Mn2)	3.16	3.16	3.13	3.22	3.16
r(Ca−Mn3)	3.50	3.50	3.30	3.19	3.25
r(Ca−Mn4)	4.47	4.37	4.22	3.71	3.78
α(CaMn[12])	58.6	59.2	58.8	58.3	59.1
α(CaMn[123])	75.6	75.5	71.3	65.3	69.2
r(Ca−O12)	2.26	2.25	2.23	2.39	2.30
r(Ca−O23)	2.35	2.36	2.33	2.31	2.33
r(Ca−O34)	2.83	2.82	2.51	2.35	2.45

residue, so further rearrangement, possibly more reflective of the other ligation differences seen between the London and Berlin structures cannot occur. As a consequence of bidentate ligation of Ala344, the position of the Ca atom in the GGA optimized structure is slightly shifted toward the amino-acid in comparison with the HDF optimized geometry, which then slightly distorts the arrangement of the Mn_4Ca cluster, exhibiting larger Ca−Mn1 and specially Ca−Mn3 and Ca−Mn4 distances (Table 2). Other less significant differences between the BP86 and B3LYP optimized structures include a slightly different arrangement of the water molecule ligated to Ca, which in turn, via hydrogen bonding, results in a slight rotation of the functional groups of Tyr161 and His190, as well as Asp170 and Arg357.

Using the ferromagnetic BP86 optimized geometry, various spin states of the WOC have been explored to find the lowest energy coupling pattern (AAAA −1332.49 eV, AAAB −1332.69 eV, AABA −1332.75 eV, ABAA −1332.53 eV, BAAA −1332.65 eV, ABBA −1332.84 eV, BBAA −1332.58 eV, BABA −1332.72 eV, where A, B indicates α, β spin, respectively). The finding that the lowest energy states are fully antiferromagnetic (spin 1/2) is consistent with our earlier calculations on isolated cluster systems,[21−24,30] as well as the experimental observation that the S_0 intermediate has a spin 1/2 ground state at low temperature.[54,55] Geometry reoptimization with the antiferromagnetic ABBA spin coupling pattern resulted in negligible changes of the cluster-protein arrangement (Table 1) and only slight modification of the cluster itself, mainly the position of the "dangling" Mn4 in relation to the other manganese atoms (Table 2).

Full reoptimization of the medium size 78 atom structures has been performed both at the GGA and HDF levels to test the influence of the protein framework on the Mn_4Ca cluster. The bidentate coordination of Ala344 to Ca in the BP86 structure is still maintained with both Ca−O distances now being equal (Table 2). On the other hand, Glu189 is no longer ligated to calcium but rather establishes hydrogen bonding to one of the water molecules. But the most dramatic effect is observed for the Mn4 atom, which now is tetrahedrally coordinated (see the Supporting Information), after losing ligation from one of two water molecules and shortening the bonding distances to single oxygens on Asp170 and Glu333. The position of Mn4 moves closer to the Ca atom and away from Mn1. In the case of the B3LYP optimized geometry, the position of Mn4 is shifted in the same direction and while it is still penta-coordinated, this occurs by Asp170 now becoming a bidentate ligand to Mn4 and Glu333 becoming monodentate to Mn3. (see the Supporting Information). Thus, we conclude that the largest observed effect of the protein framework is in determining the position of the dangling Mn(4) atom, relative to the internally rigid μ_3 oxo bridged fragment comprising the remainder of the Mn_4Ca cluster, a proposal advanced earlier.[21−23] Interestingly, several features of the freely optimized models, which started from a generally Berlin like XRD structure, now resemble the London XRD structure, particularly for the BP86 calculation. Thus the C terminal carboxylate ligates only Ca, Glu189 is singly ligated only to Mn1 and Glu333 is strongly associated with Mn4, which is ligand deficient. This has occurred within a "low" mean Mn oxidation state of <3. Although we have yet to explore these matters in greater detail, it seems reasonable to conclude that the Berlin and London XRD structures represent genuinely different forms that the protein can adopt in the region of the Mn cluster, particularly for lower Mn oxidation states (expected during crystallization), and that these differences are strongly influenced by the "internal" bonding preferences of the metal cluster components themselves.

Experimental study of the S_0 state is challenging under normal physiological conditions as three single steps are required to advance the system from the dark stable S_1 state to the S_0 state. Inevitably, imperfect flash induced turnovers result in some loss of coherence (scrambling of states), particularly in optically dense samples, which must be corrected. An "S_0*" state can be generated from dark stable S_1 by hydroxylamine[56−58] or hydrazine[58] reduction, followed by a low temperature illumination, although these chemical treatments may not necessarily lead to a physiologically relevant S_0 state. EXAFS studies of the S_0 state induced either (photo)chemically[57] or through single-flash turnover[31,59]

show higher disorder in the bond lengths in comparison with the S_1 state and heterogeneity in the Mn−Mn distances. However, the most recent data for flash advanced samples are generally consistent. Both studies[31,59] reveal two distinct Mn−Mn distances of 2.72 and 2.84−6 Å and ∼3 Mn−metal distances in the range 3.1−3.6 Å. These are modeled variously as Mn−Mn and Mn−Ca distances (difficult to distinguish above 3 Å). Robblee et al.[59] found two 2.72 and one 2.85 Å vectors, and Haumann et al.[31] found one 2.72 and one 2.84 Å vector. The present computational models are in generally good agreement with these experimental data (Table 2). The GGA optimized ferromagnetic structure exhibits two Mn−Mn distances of ca. 2.78 Å (Mn1−Mn2, Mn2−Mn3) and one of 3.05 Å (Mn3−Mn4), with the largest distance between interacting manganese atoms of 3.33 Å (Mn1−Mn3) and an average distance between Ca and three interacting Mn atoms (Mn1, Mn2, Mn3) of 3.40 Å. The overall agreement with the experimental data is better when the antiferromagnetic state is imposed, leading to an average distance of 2.75 Å between Mn1−Mn2 and Mn2−Mn3, a Mn3−Mn4 distance of 2.85 Å, and a Mn1−Mn3 distance of 3.26 Å, with the average distance between Ca and interacting Mn atoms practically unchanged. Superiority of the computational antiferromagnetic model in mimicking the experimental (cryogenic) EXAFS data is consistent with S_0 being a ground spin 1/2 state. However, the HDF calculations seem to slightly overestimate the Mn1−Mn2, Mn2−Mn3, and Mn3−Mn4 distances, while underestimating the average distance between Ca and interacting Mn atoms (3.29 Å). The overall agreement between EXAFS determined and DFT predicted metal−metal distances is slightly lower for constraint free vs partially frozen optimizations (Table 2) indicating that inclusion of the protein network, as applied in the current studies, improves the structural characteristics of the computational models of the WOC.

The excellent agreement with the experimental EXAFS data for the S_0 state, achieved specially for the GGA optimized antiferromagnetic structure, may be somewhat surprising considering that all computational models are based on the XRD structure determined with a ∼3.0 Å resolution for the dark stable S_1 state of PSII, with terminating atoms of the amino-acid groups frozen at the XRD positions. However, the overall Coulombic interaction between the cluster and the protein should not be very different between the S_1 and S_0 states as the S_0−S_1 transition is electroneutral.[60] Therefore, the structural changes of the cluster on going from the S_1 to S_0 state should be localized and caused mainly by a single Mn atom (Mn2), which changes its oxidation level from IV to III. This Mn is generally coordinatively saturated and the most "shielded" in our studies.

As suggested in our previous DFT studies on the WOC,[21−24,30] the Mn4 atom is flexible in its positioning relative to the other metal components of the cluster. Three low energy configurations are possible (designated types **I**, **II**, **III**) resembling in their metal positions the three distinct XRD structures determined by the Berlin,[11] Hyogo,[9] or London[10] groups, respectively. Further, our recent computational examination of the experimental data on substrate accessibility[23,24] and S state Mn XANES energies[30] suggests that the functional PSII center can exhibit some structural heterogeneity, which is likely lost during steady state operation of the system. Under these circumstances, our results indicate that the isolated cluster model which, by several criteria, most closely resembles the functional WOC geometry, is structure type **II** ("Hyogo like").[23] The computational models of the WOC presented here are generally intermediate between the

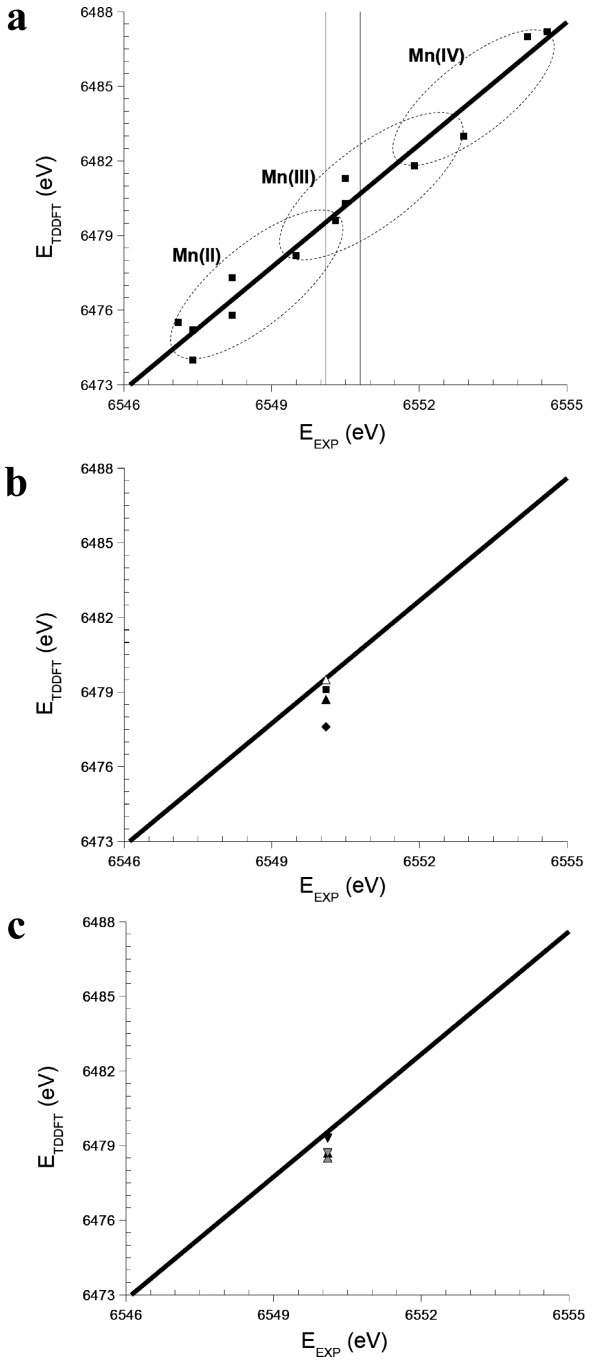

Figure 3. Relation between experimental and theoretical Mn K-edge energies for a series of Mn complexes (points) compared with the high and low energy series (see text) experimental values (solid vertical lines) for the S_0 state of PSII (a). Predicted energies for the small size (black diamond), medium size (black triangle), and large size (black square) structures derived from the GGA optimized ferromagnetic 228 atom model of the WOC and for the medium size structure (white triangle) obtained from the antiferromagnetic model (b). Predicted energies for the medium size structures derived from the 228 atom models partially optimized using the BP86 (black up-triangle) and B3LYP (black down-triangle) functional as well as freely optimized 78 atom geometries using the BP86 (gray up-triangle) and B3LYP (gray down-triangle) functionals (c). Ellipses in part a indicate ranges encompassing the same formal oxidation state of the metal in the Mn complexes. The solid line in parts a−c is the best correlation fit to the model compound data in part a (as in refs 26 and 30), and the experimental energy in parts b and c is from the low energy series.

Table 3. TDDFT Excitation Energies (in Electronvolts), Kohn−Sham Orbital Energies (in Electronvolts), and Oscillator Strengths (in Atomic Units) for Selected Transitions Calculated for the Large Size Structure Derived from the BP86 Optimized 228 Atom Ferromagnetic Model of the WOC

								final orbital composition[b] (%)			
atom	E_{TDDFT}	$f \times 10^3$	initial orbital	KSE_i	final orbital	KSE_f	electron excited[a]	Mn p-type	COO^-	COO^-	C-COO^-
Mn1	6479.65	0.39	2a	−6421.48	952a	58.15	β (0.9)	12	5	13	11
	6480.61	0.21	2a	−6421.48	957a	59.12	β	8	4	10	9
	6472.89	0.19	2a	−6421.47	900a	51.41	α	6	4	11	16
	6479.74	0.18	2a	−6421.48	953a	58.25	β	10	6	18	15
Mn2	6483.48	0.33	3a	−6421.42	979a	62.05	β	6	4	5	12
	6480.24	0.29	3a	−6421.42	956a	58.81	β	6	4	14	12
	6477.70	0.28	3a	−6421.42	939a	56.14	β	4	4	20	26
	6472.17	0.25	3a	−6421.42	894a	50.74	β	5	3	6	6
Mn3	6488.19	0.32	1a	−6421.49	1013a	66.68	β	5	5	6	9
	6487.98	0.25	1a	−6421.49	1012a	66.48	β	7	11	10	10
	6480.17	0.22	1a	−6421.48	957a	58.68	α	10	5	10	7
	6479.65	0.20	1a	−6421.49	952a	58.15	β	12	5	13	11
Mn4	6479.48	0.41	4a	−6421.21	953a	58.25	β	10	6	18	15
	6478.36	0.28	4a	−6421.19	946a	57.16	α	5	5	14	23
	6473.35	0.26	4a	−6421.21	904a	52.13	β	7	4	15	18
	6479.00	0.24	4a	−6421.21	949a	57.78	β (0.9)	13	4	8	7

[a] For mixed configurations, a contribution from a particular state is included in a description only if greater than 10%. [b] Listed orbital and atomic character values rounded up to nearest 1%.

Hyogo and Berlin types[22] (structure type **I**) but somewhat closer to the latter as a consequence of the methodology used to generate the initial structure for optimization. The Mn1−Mn4 distances of 5.29−5.46 Å (Table 2) are in the upper limit of the values predicted for the Berlin-type structures (4.2−5.5 Å in comparison with 6.1−6.8 Å for the Hyogo-type structures[22]), while the Mn[123] angles of 116.1−119.5° are higher than the average value observed for the Berlin-type structure (81−125° vs 130−160° for the Hyogo-type[22]). The Ca−Mn4 distances of 4.22−4.47 Å are between those predicted for the Berlin (3.3−3.9 Å) and Hyogo (5.1−6.4 Å) types,[22] and the same can be said for the Mn[234] angles of 142.0−145.1° (in comparison with 123−137° for Berlin and 148−156° for Hyogo types[22]). Our previous DFT results indicate that the Berlin-type arrangement is the energetically preferred geometry for isolated cluster models, while the Hyogo-type gives the best overall match between DFT results and experimental EXAFS distances for PSII.[22]

3.2. Electronic Properties. We have recently shown that TDDFT calculations performed on the optimized structures of manganese compounds produce electron transition energies that correlate very closely with the experimental Mn XANES K-edge energies of those systems.[25,26] The magnitudes of the experimental energies are offset from the theoretical values by ∼70 eV, due to a consistent error in the Mn 1s energy determined by the DFT functional used.[26] Further, the slope of the correlation line is greater than 1, as the comparison is with experimental edge positions rather than spectral peaks.[26] The edge energy variation with ligand type and geometry can be as great as the differences generated by a change of the formal Mn oxidation state, resulting in an overlapping of formal oxidation state regions, when a variety of manganese compounds is considered (Figure 3a). The experimental data for S_0 fit into the lower part of the broad Mn(III) envelope of the model compound set, irrespective of whether the PSII XANES results of Messinger et al.,[61] Iuzzolino et al.[62] ("high series"), or Roelofs et al.[63] ("low series") are used. We have shown[30] that these data sets "bracket" a range of computationally predicted energies for the model structures **I**, **II**, and **III**, throughout the S_0-S_3 sequence, with structure type **II** being consistently the lowest and corresponding closely to the low series Roelofs et al.[63] data. That characteristic which appears to distinguish structure type **II** from the others is its "openness" near Mn1, allowing ready access of a water molecule to approach along the Jahn−Teller axis direction of the Mn (which remains Mn III throughout the complete cycle to S_3). As will be discussed further below, our computed 228 atom structures retain this property, so we would expect that the low series XANES energies should be appropriate to the structures in Figure 1.

K-edge relevant excitations of 1s electrons from Mn atoms involve transitions to excited states which exhibit only a small metal p-type character[25,26] and are highly delocalized onto the ligands (Table 3). As shown earlier,[30] a compromise between computational effort and accuracy of the resulting TDDFT energies requires determination of the extent to which the computed K-edge energies are influenced by the size of the model ligating groups employed. Therefore, the 228 atom computational models of the WOC were systematically truncated (see Methodology), before electron transitions were calculated by TDDFT. Figure 2 presents three different approximations of the WOC models, with the large size structure containing the Mn_4CaO_4 cluster with ligating water molecules and Asp170, Glu333, Glu354, Asp342, Ala344, Glu189, and His332 amino-acid groups, as derived from the 228 atom ferromagnetic GGA optimized model, with reoptimization of the terminating ethyl/methyl groups. The medium size structure contains reoptimized methyl instead of ethyl moieties connected to the functional/ligating groups of the amino-acids, which in the small size structure are further reduced to hydrogen atoms only and reoptimized as well.

dx.doi.org/10.1021/jp200053n |J. Phys. Chem. B 2011, 115, 4484–4499

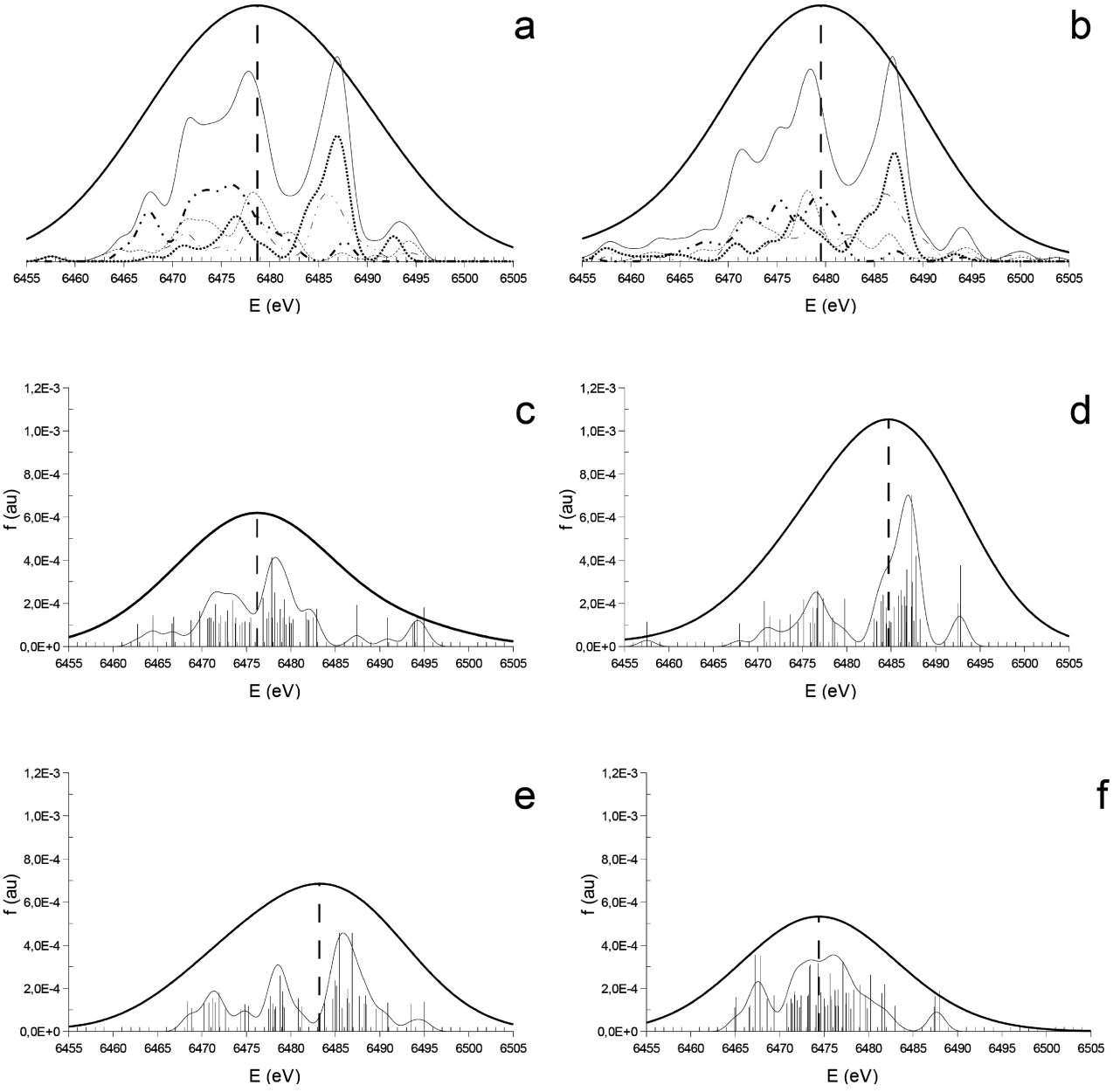

Figure 4. Total X-ray absorption spectrum envelope predicted by TDDFT for the medium size structures derived from the (a) ferromagnetic and (b) antiferromagnetic BP86 optimized 228 atom models of the WOC, plotted with the corresponding spectral component envelopes (fwhm =2.5 eV) obtained for each individual Mn atom. Manganese 1s excitations with the corresponding oscillator strengths are shown separately for the Mn1 (c), Mn2 (d), Mn3 (e), and Mn4 (f) atoms (see Scheme 1) of the medium size structure derived from the ferromagnetic BP86 optimized 228 atom model. In all cases the single broad Gaussian convolution whose maximum defines the computed mean K edge value is shown (see ref 26 for details).

The XAS measurements do not discriminate between individual Mn atoms but effectively average this property of the cluster. However, TDDFT calculations do allow one to separate contributions from each Mn atom to the final XANES spectrum (Figure 4). As revealed previously in our work,[30] although the total spectrum is a sum of all the individual transitions from the 1s orbitals of each particular Mn atom, the mean K-edge energy of the total spectrum is not simply the average of the K-edge energy values that would be inferred from the excitations of each individual Mn atom in the cluster. As excitations have different oscillator strengths, each Mn atom can have a different overall contribution to the total X-ray absorption spectrum. On the basis of our standardized method of Gaussian convolution,[26] the TDDFT transitions obtained for the large size structure yield a mean K-edge energy of 6479.1 eV for the total spectrum, which correlates very well with the experimental value[63] determined for the S_0 state of PSII, as seen on Figure 3b. On the other hand, the K-edge energy values obtained for the partial spectra of Mn1−4 are 6478.1, 6483.2, 6483.2, and 6475.3 eV, respectively (Table 4), leading to an averaged K-edge energy of 6480.0 eV. This is almost 1 eV higher than that obtained for the total spectrum. In fact, the individual energy values agree very well with the oxidation pattern of the current S_0 model (III−III−III−II), as can be seen by comparison with the appropriate areas in

dx.doi.org/10.1021/jp200053n |J. Phys. Chem. B 2011, 115, 4484–4499

Table 4. Spin Populations (in Electrons) and TDDFT Excitation Energies (in Electronvolts) Derived for Different Models and Different Structure Sizes of the WOC

	BP86 frozen						B3LYP frozen			
properties	AAAA	AAAA large	AAAA medium	AAAA small	ABBA	ABBA medium	AAAA	AAAA medium	BP86 free AAAA medium	B3LYP free AAAA medium
ρ_{spin} Mn1	3.85	3.84	3.84	3.83	3.69	3.68	3.86[a]	3.82	3.88	3.88[a]
ρ_{spin} Mn2	3.81	3.81	3.80	3.80	−3.73	−3.72	3.90[a]	3.87	3.82	3.90[a]
ρ_{spin} Mn3	3.83	3.82	3.82	3.81	−3.66	−3.65	3.84[a]	3.79	3.86	3.83[a]
ρ_{spin} Mn4	4.85	4.83	4.83	4.83	4.74	4.70	4.83[a]	4.82	4.83	4.82[a]
$\hat{S}^2$	80.860	80.865	80.866	80.866	8.372	8.356	80.752[a]	80.872	80.864	80.752[a]
total charge	−1	−1	−1	−1	−1	−1	−1	−1	−1	−1
fwhm[b] (eV)		12.5	22.5	22.5		17.5		17.5	17.5	22.5
XAS energy		6479.1	6478.7	6477.6		6479.5		6479.3	6478.5	6478.7
XAS Mn1		6478.1	6476.2	6476.0		6476.8		6477.1	6478.6	6476.8
XAS Mn2		6483.2	6484.7	6482.8		6483.6		6482.6	6483.0	6484.1
XAS Mn3		6483.2	6483.2	6484.1		6483.8		6482.6	6483.8	6481.0
XAS Mn4		6475.3	6474.4	6473.6		6475.7		6475.2	6470.0	6468.8

[a] Values derived from the B3LYP calculations using Gaussian03 package. [b] The appropriate full width at half-maximum values employed when convoluting the calculated total spectra with Gaussian functions in order to determine an edge energy corresponding to the position of the envelope maximum. The value of 20 eV was used throughout to determine edge energies of the spectral components derived for each individual Mn atom (see Figure 4).

Figure 3a. A mean K-edge energy of 6478.7 eV is predicted for the medium size structure, which still reasonably well correlates with the experimental data. Analysis of the TDDFT results reveals however slight inconsistencies between the formal oxidation states of Mn1 and Mn2 and the K-edge energies of their contributing spectra, which seem to be slightly lower than expected for the +III oxidation state of Mn1 and slightly higher than expected for Mn2. However, the value of 6477.6 eV obtained for the K-edge energy of the small size structure is 1.5 eV lower than that predicted for the large size structure, lying well off the correlation line as seen on Figure 3b. Moreover, partial K-edge energies of Mn1, Mn3, and Mn4 seem to be inconsistent with their formal oxidation states. This reflects our earlier observations on model OEC clusters,[30] where it was found that a correct chemical description of the Mn ligands, out to at least the third level of covalent attachment, was necessary for reliable computation of the TDDFT energies.

The effect of the ligand size on the TDDFT results can be rationalized by analyzing the orbital compositions of the final states to which particular electronic transitions occur. As seen in Table 3, final states possess relatively large atomic contribution from carbon atoms attached to the carboxy functional groups, as compared to the contributions from carboxylic carbon and oxygen atoms or Mn p-type orbitals. Since p-type orbitals of those carbons can mix with the π-bond system of the carboxy group, a presence or lack of them in the structural model of the WOC can affect the energies of transitions predicted by TDDFT, as described earlier.[30] The best correlation between theoretically predicted and experimentally determined K-edge energies is therefore achieved for the large size structure. However, medium size geometries seem to be a good compromise between the accuracy and feasibility of the calculations and therefore they will be applied hereafter in our studies of higher S states. It is specially true for the current studies, which deal mainly with ferromagnetic optimized structures in order to compare GGA and HDF approaches, as the energy difference of 0.4 eV between large size and medium size ferromagnetic structures of the WOC is only a half of that observed between energies from ferromagnetic and antiferromagnetic medium size geometries (Table 4). It should be noted that employing the medium size structure based on the antiferromagnetic 228 atoms GGA optimized model, which already proved to be superior by comparison with the EXAFS data, leads to only slight changes of the XANES excitation envelopes (Figure 4b vs a). However, they are sufficient to alter the K-edge energies of the contributing Mn atoms (Table 4) and shift the mean K-edge energy of the total spectrum to 6479.5 eV, which correlates superbly with experiment, as seen on Figure 3b.

Using the HDF optimized geometry for the TDDFT calculations results in a computed K-edge energy of 6479.3 eV, which is somewhat closer to the experimental value, compared to the medium size structure based on the ferromagnetic GGA optimized model (Figure 3c). Similarly to the case of the medium size structure based on the antiferromagnetic GGA optimized model, the overall consistency between the formal oxidation states of the individual Mn atoms and K-edge energies of their contributing spectra is also improved (Table 4 and Figure 3a). However, employing constraint free geometries derived at the GGA or HDF levels of theory leads to mean K-edge energies slightly less well-correlated with the experimental XANES value (Figure 3c) and a very low K-edge energy for the contributing spectrum of Mn4, which undergoes strong rearrangement of the ligation sphere, as discussed above. It can be therefore concluded that inclusion of the protein network, as applied in the current studies, improves the electronic characteristics of the computational models of the WOC, which exhibit an III−III−III−II oxidation pattern at the S_0 state, shown here to be totally consistent with the experimental XANES data. While some as yet unidentified system of higher Mn oxidation state might also properly describe the structural and electronic characteristics of the OEC in the S_0 state, to date we have found no plausible candidate, in systems derived either from the London[30] or Berlin (here) medium resolution XRD structures of PSII.

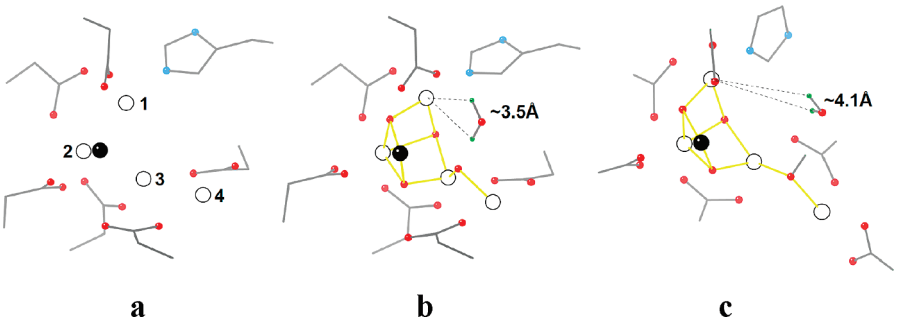

Figure 5. Geometry of the manganese cluster as determined by the XRD studies (a, ref 11, 3.0 Å Berlin), current B3LYP calculations (b), and BP86 optimizations of the singly protonated S_0 state (c, ref 23). Large white spheres Mn; large black sphere Ca; red spheres O; blue spheres N; green spheres only one water molecule is shown. The H atoms of this substrate water molecule, which approaches Mn1, and distances from Mn1 to these H atoms are indicated (see text).

3.3. Protein Matrix: Protonation and Proton Transfer. During the functional turnover of PSII, electron transfer from the WOC is weakly coupled with the proton transfer[60] steps. The resulting deprotonation of the Mn_4CaO_4 cluster and substrate water molecules can occur either before or after the oxidation step. To a limited extent, different protonation levels of the same S state may be possible. Furthermore, proton release in PSII has an oscillating pattern and is not the same on each transition in the S-cycle. The amount of uncompensated charge remains smaller than 1 throughout the S-cycle but during the $S_1 \rightarrow S_2$ transition is close to 1, indicating accumulation of net charge by the system at this stage.[60]

Several groups[13−17] have examined the available PSII XRD structures for the presence of proton, water, and oxygen channels, connecting the OEC Mn cluster to the external solvent medium (lumen). Although the results differ somewhat in detail between groups, due to methodology and protein structures used, there are some features that appear to be robustly identified. A "wide" channel, sufficient to accommodate water or methanol, leads from the Ca side of the cluster, up to and beyond the Y_Z−His190 pair and then splits into two channels before finally emerging from the protein matrix near the luminal membrane surface. On the other side of the cluster, a second channel communicates with the cluster near Mn4 and then leads away, again possibly branching just beyond the point where the Cl^- ion has been recently located.[18,19] This channel, starting at Asp61, is generally regarded as "narrow" and a likely proton channel. Near the cluster, the various channels converge to only two structures, approaching on approximately opposite sides of the Mn_4/Ca complex, a narrow pathway to Mn4 and the wide pathway leading past Ca down to Mn1,3.

The 228 atom structures examined here (Figure 1) encompass the Mn/Ca cluster, its immediate environs, and key elements of the above two channel termini, as they lead to the cluster. We have not yet included the recently discovered Cl^- in the narrow channel, as its position is still somewhat uncertain, but it appears to be located near the ε amino group of D2−Lys317, which in our calculations forms a salt bridge with Glu65. A detailed study of the role of anions in the narrow channel and elsewhere will be presented separately. Because we favor the low Mn oxidation state paradigm for the WOC cluster, only a minimum of additional components, not revealed by the crystal structures, is required to ensure the metal cluster is locally at or near charge neutrality when embedded in the protein matrix. Thus, assuming all caboxylate ligands are anionic, only four additional oxo groups are required for a charge neutral state in S_1. Further, consistent with the above channel studies, we find that only five water molecules can be accommodated within the immediate environs of the cluster (Figure 1), mostly in the wide channel region between the cluster and Y_Z. One water, essentially on the opposite side of the cluster near the entrance to the narrow channel, is located near the only position so far identified by XRD as a possible water site.[14]

The structures in Figure 1, particularly Figure 1b (B3LYP), closely resemble the metal ion and water dispositions in the functionally favored structures (type **II**) previously identified from our studies on freely optimized, isolated complexes.[21−24] Up to two waters are associated with Mn4 (at least in S_0), one with Ca, one with Ca/Mn3, and one in a "cleft" giving access to Mn1 (see Figure 5b,c). The latter two waters we proposed, by several criteria, to be the substrate water molecules.[23,24] In fact, inclusion of the local protein framework results in the cleft water now approaching Mn1 in such a way that the proton−Mn distances are close to those inferred from ESEEM studies on the functionally generated S_0 state.[64] In the isolated model complex for S_0, this approach is structurally permitted but does not occur in the energy minimized configuration due to local H-bonding preferences (Figure 5).

The S_0 structures examined here all have net charge −1 (i.e., 0 in S_1). We have recently shown[23,24] that a charge neutralized (protonated) version of the S_0 state (Figure 5c) is most consistent with data on water exchange and substrate access to Mn1. Although the antiferromagnetic (ABBA) 228 atom GGA optimized III−III−III−II oxidation state model of the WOC described here is in excellent agreement with both EXAFS and XANES data for the S_0 state of PSII, it is appropriate to test how protonation of the structure can affect its electronic and structural characteristics. HDF optimizations of a series of protonated models containing 229 atoms have been performed. TDDFT calculations on the resulting medium size structures derived from the ferromagnetic optimized models are compared with the TDDFT energy of 6479.3 eV for the corresponding unprotonated 228 atom model of the S_0 state, which has an energy only 0.2 eV lower in value than that predicted for the most favorable antiferromagnetic model (Table 4).

Initial single protonation of either water molecule ligated to Mn4 leads to deligation of the water, while initial protonation of the water ligated to Ca results in a structure with the carboxylic group of Asp170 protonated and completely deligated from the Mn4 atom. A proton initially attached to either of the two

dx.doi.org/10.1021/jp200053n |*J. Phys. Chem. B* 2011, 115, 4484–4499

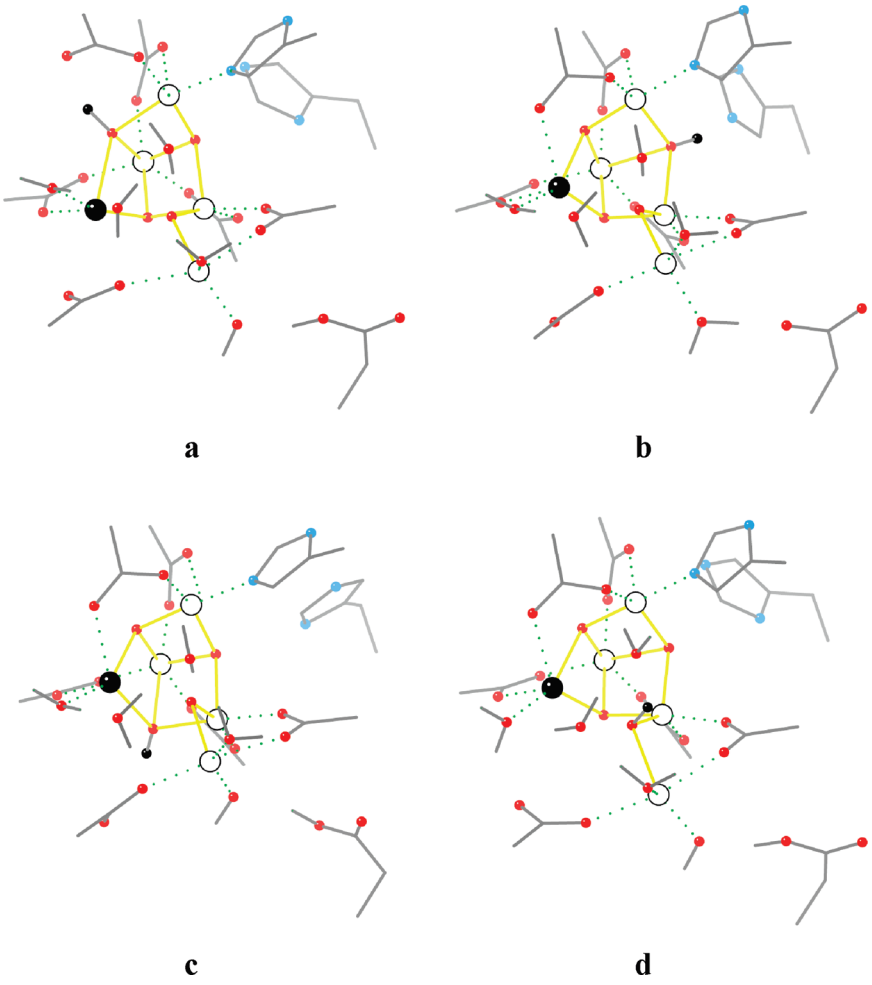

Figure 6. B3LYP optimized 229 atom structures (simplified and reduced to the metal cluster region of the system for clarity) of the four lowest energy models of the WOC at the S_0 state, singly protonated at the Mn1−O−Mn2 oxo bridge (a), Mn1(Mn2)−O−Mn3 oxo bridge (b), Mn2−O−Mn3 oxo bridge (c), and Mn3−O−Mn4 oxo bridge (d). Large white spheres Mn; large black sphere Ca; red spheres O; blue spheres N; black spheres H atoms of the hydroxyl groups formed.

remaining water molecules (i.e., the substrate waters) results in protonation of the Mn3−O−Mn4 oxo bridge, which also takes place when H^+ is initially attached to the second water molecule ligating Mn4 (i.e., that contacting the wide channel and not located in the XRD structure). These three final structures containing a hydroxyl instead of oxo bridge between Mn3 and Mn4 are energetically more favorable than the remaining two, and their total energies are within a 50 kJ mol^{-1} range, with the lowest energy geometry shown in Figure 6d. Single protonation of the three remaining oxo bridges results in somewhat more energetically favorable geometries, as seen in Figure 6a−c and in Table 5. Stabilization of the structure containing an hydroxyl group between Mn1 and Mn2 is achieved by creating a hydrogen bond with the carboxylic group of nearby Glu189 and deligating this amino-acid from Ca. A lowering of the total energy for the structure with a protonated μ_3-oxo bridge between Mn1, Mn2, and Mn3 derives from hydrogen bonding with the nitrogen atom of His337. By comparison, initial single protonation of the three carboxylic groups singly ligated to Mn atoms of the cluster leads to the energetically least favorable structures, with Glu189 protonated and deligated from both Mn1 and Ca, Ala344 protonated but still ligated to both Mn2 (2.34 Å) and Ca (2.73 Å), or Asp170 protonated and deligated in exactly the same way as when initial protonation of the water ligated to Ca occurred (see the Supporting Information). The mean Mn K-edge TDDFT energies for the four most stable singly protonated models of the S_0 state are collected in Table 5. For the models with an hydroxyl group between Mn2 and Mn3 or between Mn3 and Mn4, basically no change is observed by comparison with the energy determined for the unprotonated model. On the other hand, the values determined for the other two models are downshifted by ca. 0.8 eV. The structure containing a protonated μ_3-oxo bridge connecting Mn1, Mn2, and Mn3 has the lowest TDDFT energy, but this might in part be due to exclusion of His337 from the TDDFT calculations. Inclusion of this group may be important for a proper description of the XANES characteristics here, as the imidazole N of the side chain creates a hydrogen bond with the μ_3-hydroxyl moiety in question. The mean Mn K-edge energies derived from the TDDFT calculations are in reasonable accord with the experimental values for all four models (Figure 7), with the values obtained for the two higher energy structures lying closest to the correlation line. Thus the TDDFT calculations alone do not exclude or support the validity of any of the four protonation schemes studied.

Although the HDF structures (Figure 2b) are generally less close to the experimental EXAFS derived metal−metal distances

dx.doi.org/10.1021/jp200053n |J. Phys. Chem. B 2011, 115, 4484–4499

Table 5. Structural Properties (Bond Lengths in Angstroms, Angles in Degrees), Spin Populations (in Electrons), Relative Energies (in Kilojoules Per Mole) and TDDFT Excitation Energies (in Electronvolts) Derived for the Singly Protonated Models of the Manganese Cluster

properties	B3LYP frozen O12−H^+ AAAA	B3LYP frozen O123−H^+ AAAA	B3LYP frozen O23−H^+ AAAA	B3LYP frozen O34−H^+ AAAA
r(Mn1−Mn2)	2.91	2.97	2.76	2.87
r(Mn2−Mn3)	2.90	2.93	3.03	2.88
r(Mn1−Mn3)	3.44	3.48	3.43	3.38
r(Mn3−Mn4)	3.23	3.12	2.89	3.31
r(Mn1−Mn4)	5.72	5.55	5.30	5.95
α(Mn[123])	72.6	72.3	72.6	72.0
α(Mn[234])	140.1	140.7	140.5	142.6
α(Mn[134])	118.2	114.4	113.6	125.6
α(Mn[1234])	92.2	85.8	78.7	103.4
r(Ca−Mn1)	3.98	3.54	3.42	3.50
r(Ca−Mn2)	3.34	3.21	3.30	3.15
r(Ca−Mn3)	3.24	3.35	3.44	3.41
r(Ca−Mn4)	3.93	4.18	4.08	4.61
α(CaMn[12])	55.3	58.3	63.6	58.2
α(CaMn[123])	64.0	70.3	70.3	73.1
r(Ca−O12)	2.38	2.31	2.29	2.24
r(Ca−O23)	2.33	2.38	2.39	2.33
r(Ca−O34)	2.33	2.51	2.53	2.70
ρ_{spin} Mn1	3.88	3.88	3.92	3.86
ρ_{spin} Mn2	3.90	3.90	3.88	3.92
ρ_{spin} Mn3	3.89	3.89	3.84	3.83
ρ_{spin} Mn4	4.82	4.84	4.83	4.84
$\hat{S}^2$	80.752	80.752	80.752	80.752
ΔE (kJ/mol)	0.0	29.1	33.8	67.5
fwhm (eV)	20.0	22.5	15.0	17.5
TDDF (eV)	6478.6	6478.5	6479.3	6479.2

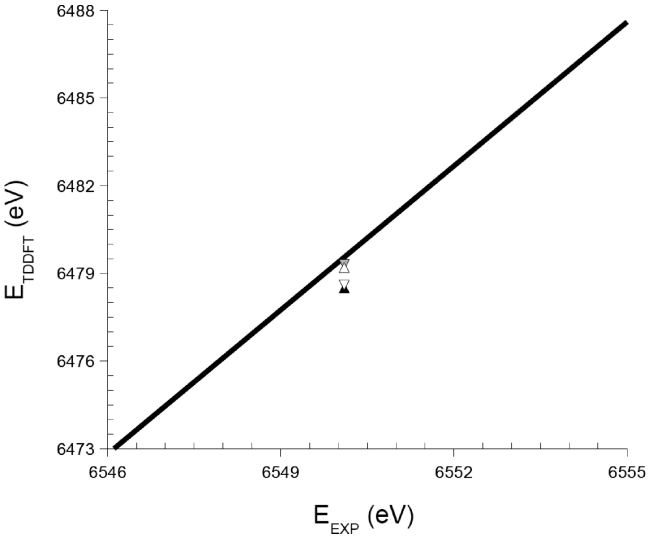

Figure 7. Relation between experimental and theoretical Mn K-edge energies predicted for the medium size structures derived from the B3LYP optimized 229 atom models of the WOC at the S_0 state. Singly protonated at the Mn1−O−Mn2 oxo bridge (white down-triangle), Mn1(Mn2)−O−Mn3 oxo bridge (black up-triangle), Mn2−O−Mn3 oxo bridge (gray down-triangle), and Mn3−O−Mn4 oxo bridge (white up-triangle). Solid line as in Figure 3.

than the antiferromagnetic GGA structures (Figure 2a, Table 2), we are concerned here principally with examining the structural *changes* resulting from protonation at various locations, for which the HDF methodology is expected to be reliable. Comparing the structure exhibiting an hydroxyl bridge between Mn1 and Mn2 with the HDF optimized unprotonated model (Table 2), the Mn1−Mn2 and Mn2−Mn3 distances are slightly elongated, while the Mn3−Mn4 distance increases by 0.11 Å. Additionally, strong heterogeneity is observed in the distances between calcium and the interacting manganese atoms, with an average Ca−Mn separation of 3.52 Å and a Ca−Mn1 distance of 3.98 Å. The model containing the μ_3-hydroxyl bridge connecting Mn1, Mn2, and Mn3 exhibits slightly elongated Mn1−Mn2 and Mn2−Mn3 as well as Mn1−Mn3 distances (by ∼0.08 and 0.18 Å, respectively). Single protonation of the Mn2−O−Mn3 oxo bridge favorably reduces the Mn3−Mn4 separation to 2.89 Å, but unfavorably increases the Mn2−Mn3 distance significantly. In total, this single model is the most different from the unprotonated structure, as compared to other protonated geometries (Table 5). The structure with an hydroxyl bridge between Mn3 and Mn4, even if showing almost no change in the Mn1−Mn2 and Mn2−Mn3 distances, is characterized by a large Mn3−Mn4 separation of 3.31 Å, similar to the Mn1−Mn3 distance of 3.38 Å. It seems that overall, those variants with the singly protonated Mn1−O−Mn2 and Mn3−O−Mn4 oxo bridges are most similar to the unprotonated geometry, particularly in regard

dx.doi.org/10.1021/jp200053n |*J. Phys. Chem. B* 2011, 115, 4484–4499

Table 6. Comparison of Mn−Mn Distances (Å) Derived from EXAFS and Those Predicted by Present and Other Computational Studies

properties	BP86 frozen ABBA[a]	B3LYP frozen AAAA[a]	Batista et al S_0 model[b]	Seigbahn S_0^{-1} model[c]	Seigbahn S_0^{-2} model[c]	EXAFS Mn−Mn vectors for S_0[d]
r(Mn1−Mn2)	2.72	2.87	2.65	2.87	2.86	
r(Mn2−Mn3)	2.78	2.87	2.96	2.86	2.87	
r(Mn1−Mn3)	3.26	3.30	2.92	3.08	2.99	(1−2) × 2.72
r(Mn3−Mn4)	2.85	3.12	3.04	2.86	2.88	1 × 2.85
r(Mn1−Mn4)	5.29	5.46	3.79	4.46	4.48	(1−2) × 3.1−3.3

[a] Present studies. [b] From ref 66. The calculation is for the antiferromagnetic ground state. [c] From ref 34. The calculation is for a full ferromagnetic state. [d] From refs 31 and 61 for EXAFS of unoriented PSII (higher plant). Indicated are numbers of vectors and lengths, or length ranges.

to the well-resolved EXAFS parameters, suggesting some preference for assigning the putative single protonation to those positions. However, it should be noted that these protonations of the corresponding 228 atom model do not result in any significant improvement in the structural or electronic parameters of the S_0 state, based on comparison with the experimental XANES or EXAFS data.

Single protonations at different sites within the WOC resulted in a variety of different ligation patterns, as noted above (and see the Supporting Information). It is perhaps surprising that all ten final models still exhibit the same III−III−III−II Mn oxidation scheme, despite some sensitivity of the oxidation pattern to the structural arrangement, number of ligated water molecules, and even protonation level observed previously in studies of the isolated complex models.[22−24] Additionally, in seven of ten structures examined, a proton is transferred from the OEC to the carboxy group of Asp61, which is located near the Mn4 atom, maintaining practically the same total charge of the WOC core (Mn_4CaO_4 cluster, ligating water molecules and 7 ligating amino-acids), as before the single protonation. In six of those seven geometries, the dangling manganese atom (Mn4) is ligated by one water molecule and one hydroxyl group, the latter near the XRD identified putative water position. This is highly suggestive of a proposal we have made earlier,[24,30] namely that a proton from this water molecule on Mn4 is released to the narrow proton channel, starting near Asp61, to effect charge compensation in the cluster during S state turnover.

4. COMPARISONS WITH OTHER RECENT COMPUTATIONAL PSII MODELS

Two other groups have recently presented detailed computational models of the OEC in the metastable S states, including S_0, which incorporate significant elements of the local protein matrix. Batista and co-workers[65−67] have developed large QM−MM models of the OEC, in a protein environment closely based on the 3.5 Å XRD London structure.[10] These are, in total atoms (∼2000) and water molecules (85) the largest PSII WOC models yet attempted, although most components outside the central $CaMn_4O_4$cluster core and immediate ligands were treated by molecular mechanics using the AMBER MM force field. Seigbahn[33−35] has used an approach similar to ours, modeling the Mn cluster core and immediate ligands fully with high level QM (∼150 atoms), with the amino-acid α carbons fixed in the relative positions of the London XRD structure, but with a metal ligation pattern much closer to that of the more recent 2.9, 3.0 Å Berlin structures, as used here. We have recently reviewed[68] PSII computational studies published over the past decade by all groups in the field, and it seems now clear that the Berlin like structures of the immediate cluster region are more energetically reasonable[21,35] and consistent with recent spectroscopic data.[68]

The main difference between our approach and that of other computational groups[33−35,65−67,69] modeling the OEC is our assignment of a lower mean oxidation state to the Mn cluster during functional turnover.[23,30] This ranges from 2.75 in S_0 to 3.75 in S_3. That assumed elsewhere is 3.25 in S_0, with electrons subsequently removed initially from Mn but sometimes from ligands as well. This difference might manifest structurally, as well as in the predicted XANES energies for the S_0 models. Table 6 compares Mn−Mn distances from Table 2 for the matrix frozen geometries of antiferromagnetic and ferromagnetic cluster configurations, with the corresponding distances from the Batista and Seigbahn S_0 structures. Shown also are the consensus EXAFS Mn−Mn vector lengths, below 3.3 Å, for the higher plant S_0 state generated by flash advancement of unoriented samples. It is now apparent from crystal structures and modeling that most, if not all OEC Mn−metal distances below 3.4 Å are Mn−Mn distances. One sees, consistent with our above discussion, that our antiferromagnetic cluster model fits the data well, significantly better than the three other models (Table 6). Part of the discrepancy in the Seigbahn case may arise from the use of a full ferromagnetic calculation (compare our ABBA and AAAA cases), but not for the Batista cluster structure, which is antiferromagnetic and probably least consistent with the data. Thus the lower oxidation state paradigm used here, with inclusion of protein constraints, leads to Mn−Mn distances generally in very good agreement with the EXAFS data and even elaborate computational models like the QM/MM studies—which in theory should mimic both protein-cluster interactions as well as structural and electronic characteristics of the WOC—lead to a set of Mn−Mn distances merely consistent with experiment. In S_1, these needed to be semiempirically reoptimized to match with the EXAFS data.[67] The close agreement between the ferromagnetically calculated AAAA and Seigbahn structures for the Mn1−Mn2 and Mn2−Mn3 distances probably reflects the basically similar ligation arrangement and oxidation patterns in the two cases (III−III−III and III−III−IV, respectively).

Batista et al. have also examined water and proton channels in their models. Because the arrangement of protein supplied ligation is different in their model and ours (particularly Glu333 ligates Mn1 and Mn3, rather than Mn3 and Mn4, as in the Berlin type structures), Mn4 is now significantly further from Asp61 than is the case in Figure 1 and the direct proton "shift" we infer to occur between these groups at the entrance of the proton channel would not occur (see Figure 6). In the Batista model, Asp61 interacts directly with Glu65 through two intervening

water molecules. This detailed arrangement of the two amino acids depicted by Batista et al. is unlikely to occur in the actual PSII protein, as Cl^- is now known to approximately occupy this position[18,19] and not be ligated to Ca, as in the QM/MM models. We find the putative proton shift identified in Figure 6 to be very suggestive, in terms of both structure and possible mechanism, but a resolution of this must await further studies.

5. CONCLUSIONS

The largest models of the WOC yet calculated by pure DFT methods have been constructed based on the XRD structure of PSII determined with 2.9−3.0 Å resolution. The BP86 approach seems to slightly outperform B3LYP hybrid density functional determination of the structural parameters, with the best overall agreement between computationally predicted and experimentally determined metal−metal distances found for the GGA optimized 228 atom ABBA antiferromagnetic structure. The same model, exhibiting a III−III−III−II Mn oxidation pattern, leads to a TDDFT predicted mean K-edge energy which superbly correlates with the low energy XANES experimental value determined for the S_0 state of PSII. Single protonation of the model, resulting in overall charge neutrality for the system, does not generally improve the structural or electronic parameters of the modeled S_0 state, by comparison with the experimental XANES or EXAFS data. However, our studies reveal several factors of potential significance for the WOC function during S state turnover, some of which we have suggested previously from calculations on isolated cluster models. These specifically include:

(1) The III−III−III−II oxidation state pattern for Mn1 to Mn4 in S_0 appears to be robust, when the local protein structure constraints are included in the modeling. We previously identified[29] this as the favored pattern for that class of isolated WOC model complexes (type **II**) deemed most likely to correspond to the functional active site. This implies that the S_4 state would have an oxidation level of at most Mn $(IV)_3$ (III), which is somewhat below that frequently believed necessary for water oxidation, based on model compound experience.[70] However, an examination of relevant redox potential data (Supporting Information S7) indicates that there appears to be no fundamental *thermodynamic* limitation to water oxidation occurring at the lower Mn redox levels, within a sequence likely operating in the WOC. Rather Mn appears to be uniquely suited, among common transition metals, for this purpose. Remarkably, there is little difference thermodynamically in Mn operating between mean oxidation levels of 3.0 to 4.0. The unique efficiency of the WOC will then turn upon the manner in which transition state energies for O−O bond formation are lowered, so that the effective reaction "overpotential" is less than ∼200 mV. Defining this mechanism will clearly be challenging.

(2) If a proton is transferred from a water molecule to the cluster, this occurs preferentially onto the oxo bridge connecting Mn3 and Mn4. We have previously suggested this process occurs spontaneously in S_1,[30] resulting in the substrate water bound to Ca/Mn3 becoming an hydroxide and so having a much slower exchange rate than in the other isolatable S states (where it is water).

(3) If the metal cluster is locally neutral through protonation in S_0, then the most likely positions, in terms of consistency with the XANES and EXAFS data, are those locations which minimally alter the electronic/structural properties of the unprotonated structures. These are the μ_2-oxo bridges connecting Mn1,2 and Mn3,4. This matter is now under examination.

(4) A very significant finding is that a *natural* deprotonation pathway for the cluster, to reduce local positive charge increase, is from the water on Mn4 adjacent to the proton channel starting with Asp61 and including Lys317, Glu65, Arg334, Glu312, as well as a likely Cl^- ion. We have proposed that this pathway operates in S_3,[30] to charge compensate on the $S_2 \rightarrow S_3$ transition. Although the present study is confined to S_0, where we do not expect the channel to be functionally utilized in this way, the proton insertions examined here can be regarded as "probes" of the system's response to an induced "excess" of local positive charge in the cluster. What we then see is a generally consistent transfer of a proton into the "mouth" (Asp61) of the putative proton exit channel.

Finally, although Tyr161 and His190 have been included in the current model and show some rotational flexibility, they do not significantly affect the structural or electronic properties of the Mn_4Ca cluster in the S_0 state. The structures in Figure 1 show that there is a clear potential for a H-bond connected pathway, through two water molecules, from the phenoxyl group on Y_Z to the Mn cluster. However, no propensity for proton exit along this pathway is seen in the present studies. This suggests that if such a process occurs, it is probably correlated with electron transfer to the $Y_Z^{\bullet}$ radical species, after it has transferred its phenoxyl proton to His190. The inclusion of such effects may be important in a detailed description of electron transfer from the cluster or electronic and functional characteristics of the higher S states. At present, our computational model shows excellent agreement with the experimental XANES and EXAFS data, even without inclusion of the Cl^- ion. As chloride is located around 6.5−7.4 Å from the Mn_4Ca cluster, somewhere close to D2-Lys317 or D1-Asn338/CP43-Glu354, its direct involvement in the water oxidizing process is highly unlikely. However, it can play an important role in the proton transfer within and from the WOC.

■ ASSOCIATED CONTENT

Supporting Information. Optimized structures (*XYZ* coordinates) of the WOC models and calculated TDDFT excitation energies for transitions with an oscillator strength higher than 10^{-4} au. Summary of relevant redox potential data for selected transition metals. This material is available free of charge via the Internet at http://pubs.acs.org.

■ AUTHOR INFORMATION

Corresponding Author

*E-mail: Ron.Pace@anu.edu.au. Phone: +61-(0)2-61254546. Fax: +61-(0)2-61258997.

■ ACKNOWLEDGMENT

The authors gratefully acknowledge financial assistance from the Australian Research Council. The computations were performed using the platforms of the Australian

Partnership for Advanced Computing, operating through the Australian National University Supercomputer Facility, and of the Wroclaw Center of Networking and Supercomputing (Grant No. 48).

REFERENCES

(1) Yachandra, V. K.; Sauer, K.; Klein, M. P. *Chem. Rev.* **1996**, *96* 2927–2950.
(2) Renger, G. *Biochim. Biophys. Acta* **2001**, *1503*, 210–228.
(3) McEvoy, J. P.; Brudvig, G. W. *Chem. Rev.* **2006**, *106*, 4455–4483.
(4) Kok, B.; Forbush, B.; McGloin, M. *Photochem. Photobiol.* **1970**, *11*, 457–475.
(5) Dau, H.; Iuzzolino, L.; Dittmer, J. *Biochim. Biophys. Acta* **2001**, *1503*, 24–39.
(6) Chu, H.-A.; Hillier, W.; Law, N. A.; Babcock, G. T. *Biochim. Biophys. Acta* **2001**, *1503*, 69–82.
(7) Peloquin, J. M.; Britt, R. D. *Biochim. Biophys. Acta* **2001**, *1503* 96–111.
(8) Hillier, W.; Wydrzynski, T. *Biochim. Biophys. Acta* **2001**, *1503* 197–209.
(9) Kamiya, N.; Shen, J.-R. *Proc. Natl. Acad. Sci. U.S.A.* **2003**, *100* 98–103.
(10) Ferreira, K. N.; Iverson, T. M.; Maghlaoui, K.; Barber, J.; Iwata, S. *Science* **2004**, *303*, 1831–1939.
(11) Loll, B.; Kern, J.; Saenger, W.; Zouni, A.; Biesiadka, J. *Nature* **2005**, *438*, 1040–1044.
(12) Kuzek, D.; Pace, R. J. *Biochim. Biophys. Acta* **2001**, *1503* 123–137.
(13) Gabdulkhakov, A.; Guskov, A.; Broser, M.; Kern, J.; Müh, F.; Saenger, W.; Zouni, A. *Structure* **2009**, *17*, 1223–1234.
(14) Guskov, A.; Kern, J.; Gabdulkhakov, A.; Broser, M.; Zouni, A.; Saenger, W. *Nature Struct. Mol. Biol.* **2009**, *16*, 334–342.
(15) Murray, J. W.; Barber, J. *J. Strut. Biol.* **2007**, *159*, 228–237.
(16) Ishikita, H.; Saenger, W.; Loll, B.; Biesiadka, J.; Knapp, E.-W. *Biochemistry* **2006**, *45*, 2063–2071.
(17) Ho, F. M.; Styring, S. *Biochim. Biophys. Acta* **2008**, *1777* 140–153.
(18) Murray, J. W.; Maghlaoui, K.; Kargul, J.; Ishida, N.; Lai, T.-L.; Rutherford, A. W.; Sugiura, M.; Boussac, A.; Barber, J. *Energy Environ. Sci.* **2008**, *1*, 161–166.
(19) Kawakami, K.; Umena, Y.; Kamiya, N.; Shena, J.-R. *Proc. Natl. Acad. Sci. U.S.A.* **2009**, *106*, 8567–8572.
(20) Yocuma, C. F. *Coord. Chem. Rev.* **2008**, *252*, 296–305.
(21) Petrie, S.; Stranger, R.; Gatt, P.; Pace, R. J. *Chem.—Eur. J.* **2007**, *13*, 5082–5089.
(22) Petrie, S.; Stranger, R.; Pace, R. J. *Chem.—Eur. J.* **2008**, *14* 5482–5494.
(23) Petrie, S.; Stranger, R.; Pace, R. J. *Angew. Chem.* **2010**in press.
(24) Petrie, S.; Stranger, R.; Pace, R. J. *Chem.—Eur. J.* **2010**in press.
(25) Jaszewski, A. R.; Stranger, R.; Pace, R. J. *J. Phys. Chem. A* **2008**, *112*, 11223–11234.
(26) Jaszewski, A. R.; Stranger, R.; Pace, R. J. *Phys. Chem. Chem. Phys.* **2009**, *11*, 5634–5642.
(27) Stemmler, T. L.; Sossong, T. M., Jr.; Goldstein, J. I.; Ash, D. E.; Elgren, T. E.; Kurtz, D. M., Jr.; Penner-Hahn, J. E. *Biochemistry* **1997**, *36*, 9847–9858.
(28) Gunter, T. E.; Miller, L. M.; Gavin, C. E.; Eliseev, R.; Salter, J.; Buntinas, L.; Alexandrov, A.; Hammond, S.; Gunter, K. K. *J. Neurochem.* **2004**, *88*, 266–280.
(29) Gunter, K. K.; Aschner, M.; Miller, L. M.; Eliseev, R.; Salter, J.; Anderson, K.; Gunter, T. E. *Neurobiol. Aging* **2006**, *27*, 1816–1826.
(30) Jaszewski, A. R.; Stranger, R.; Pace, R. J. *Chem.—Eur. J.* **2011**in press.
(31) Haumann, M.; Müller, C.; Liebisch, P.; Iuzzolino, L.; Dittmer, J.; Grabolle, M.; Neisius, T.; Meyer-Klaucke, W.; Dau, H. *Biochemistry* **2005**, *44*, 1894–1908.
(32) Zein, S.; Kulik, L. V.; Yano, J.; Kern, J.; Pushkar, Y.; Zouni, A.; Yachandra, V. K.; Lubitz, W.; Neese, F.; Messinger, J. *Phil. Trans. R. Soc. B* **2008**, *363*, 1167–1177.
(33) Siegbahn, P. E.M. *Phil. Trans. R. Soc. B* **2008**, *363*, 1221–1228.
(34) Siegbahn, P.E. M. *Chem.—Eur. J.* **2008**, *14*, 8290–8302.
(35) Siegbahn, P.E. M. *J. Am. Chem. Soc.* **2009**, *131*, 18238–18239.
(36) Dau, H.; Grundmeier, A.; Loja, P.; Haumann, M. *Phil. Trans. R. Soc. B* **2008**, *363*, 1237–1244.
(37) Thompson, M. A. *ArgusLab 4.0.0*; Planaria Software LLC: Seattle WA, 2004.
(38) Yano, J.; Kern, J.; Irrgang, K.-D.; Latimer, M. J.; Bergmann, U.; Glatzel, P.; Pushkar, Y.; Biesiadka, J.; Loll, B.; Sauer, K.; Messinger, J.; Zouni, A.; Yachandra, V. K. *Proc. Natl. Acad. Sci. U.S.A.* **2005**, *102*, 12047–12052.
(39) Te Velde, G.; Bickelhaupt, F. M.; Baerends, E. J.; Fonseca Guerra, C.; van Gisbergen, S. J. A.; Snijders, J. G.; Ziegler, T. *J. Comput. Chem.* **2001**, *22*, 931–967.
(40) Vosko, S. H.; Wilk, L.; Nusair, M. *Can. J. Phys.* **1980**, *58* 1200–1211.
(41) Becke, A. D. *Phys. Rev. A* **1988**, *38*, 3098–3100.
(42) Perdew, J. P. *Phys. Rev. B* **1986**, *33*, 8822–8824.
(43) van Lenthe, E.; Baerends, E. J. *J. Comput. Chem.* **2003**, *24* 1142–1156.
(44) van Lenthe, E.; Ehlers, A.; Baerends, E. J. *J. Chem. Phys.* **1999**, *110*, 8943–8953.
(45) Frisch, M. J., et al. *Gaussian 03, Rev. E.01*; Gaussian, Inc.: Wallingford CT, 2004.
(46) Becke, A. D. J. *Chem. Phys.* **1993**, *98*, 5648–5652.
(47) Wachters, A. J. H. J. *Chem. Phys.* **1970**, *52*, 1033.
(48) Bauschlicher, C. W., Jr.; Langhoff, S. R.; Barnes, L. A. *J. Chem. Phys.* **1989**, *91*, 2399.
(49) Godbout, N.; Salahub, D. R.; Andzelm, J.; Wimmer, E. *Can. J. Chem.* **1992**, *70*, 560.
(50) Dunning, Jr., T. H.; Hay, P. J. *Modern Theoretical Chemistry*; Plenum: New York, 1976; Vol. 3, p 1.
(51) Gross, E. K. U.; Kohn, W. *Adv. Quant. Chem.* **1990**, *21* 255–291.
(52) Strickler, M. A.; Walker, L. M.; Hillier, W.; Debus, R. J. *Biochemistry* **2005**, *44*, 8571–8577.
(53) Stull, J. A.; Stich, T. A.; Service, R. J.; Debus, R. J.; Mandal, S. K.; Armstrong, W. H.; Britt, R. D. *J. Am. Chem. Soc.* **2010**, *132*, 446–447.
(54) Åhrling, K. A.; Peterson, S.; Styring, S. *Biochemistry* **1998**, *37*, 8115–8120.
(55) Kulik, L. V.; Epel, B.; Lubitz, W.; Messinger, J. *J. Am. Chem. Soc.* **2005**, *127*, 2392–2393.
(56) Guiles, R. D.; Yachandra, V. K.; McDermott, A. E.; Cole, J. L.; Dexheimer, S. L.; Britt, R. D.; Sauer, K.; Klein, M. P. *Biochemistry* **1990**, *29*, 486–496.
(57) Riggs-Gelasco, P. J.; Mei, R.; Yocum, C. F.; Penner-Hahn, J. E. *J. Am. Chem. Soc.* **1996**, *118*, 2387–2399.
(58) Messinger, J.; Nugent, J. H. A.; Evans, M. C. W. *Biochemistry* **1997**, *36*, 11055–11060.
(59) Robblee, J. H.; Messinger, J.; Cinco, R. M.; McFarlane, K. L.; Fernandez, C.; Pizarro, S. A.; Sauer, K.; Yachandra, V. K. *J. Am. Chem. Soc.* **2002**, *124*, 7459–7471.
(60) Rappaport, F.; Lavergne, J. *Biochim. Biophys. Acta* **2001**, *1503* 246–259.
(61) Messinger, J.; Robblee, J. H.; Bergmann, U.; Fernandez, C.; Glatzel, P.; Visser, H.; Cinco, R. M.; McFarlane, K. L.; Bellacchio, E.; Pizarro, S. A.; Cramer, S. P.; Sauer, K.; Klein, M. P.; Yachandra, V. K. *J. Am. Chem. Soc.* **2001**, *123*, 7804–7820.
(62) L. Iuzzolino, L.; J. Dittmer, J.; W. Dörner, W.; W. Meyer-Klaucke, W.; H. Dau, H. *Biochemistry* **1998**, *37*, 17112–17119.
(63) Roelofs, T. A.; Liang, W.; Latimer, M. J.; Cinco, R. M.; Rompel, A.; Andrews, J. C.; Sauer, K.; Yachandra, V. K.; Klein, M. P. *Proc. Natl. Acad. Sci. U.S.A.* **1996**, *93*, 3335–3340.
(64) Åhrling, K. A.; Evans, M. C. W.; Nugent, J. H. A.; Ball, R. J.; Pace, R. J. *Biochemistry* **2006**, *45*, 7069–7082.

(65) Sproviero, E. M.; Gascón, J. A.; McEvoy, J; P.; Brudvig, G. W.; Batista, V. S. *J. Chem. Theory Comput.* **2006**, *2*, 1119–1134.
(66) Sproviero, E. M.; Gascón, J. A.; McEvoy, J; P.; Brudvig, G. W.; Batista, V. S. *J. Am. Chem. Soc.* **2008**, *130*, 3428–3442.
(67) Sproviero, E. M.; Gascón, J. A.; McEvoy, J; P.; Brudvig, G. W.; Batista, V. S. *J. Am. Chem. Soc.* **2008**, *130*, 6728–6730.
(68) Gatt, P.; Stranger, R.; Pace, R. J. *J. Photochem. Photobiol. B: Biol.*, in press.
(69) Kusonoki, M. *Biochim. Biophys. Acta* **2007**, *1767*, 484–492.
(70) McEvoy, J. P.; Brudvig, G. W. *Chem. Rev.* **2006**, *106*, 4455–4483.